GFZ

Helmholtz-Zentrum
POTSDAM

Key Points:
- We present the detailed images of the LAB beneath the NE Tibetan Plateau using S receiver functions
- The marked LAB steps occur at 130 +/- 10 km away from the boundary faults between the NE Tibetan Plateau to the surrounding blocks
- The asthenospheric flow leads to the delamination of fragmented mantle lithosphere beneath southern edges of the Alxa and Ordos blocks

Seismic Evidence for Lateral Asthenospheric Flow Beneath the Northeastern Tibetan Plateau Derived From *S* Receiver Functions

Qiang Xu[1,2] [ID], Shunping Pei[1] [ID], Xiaohui Yuan[3] [ID], Junmeng Zhao[1,2], Hongbing Liu[1,2], Hongwei Tu[4], and Shuze Chen[1]

[1]Key Laboratory of Continental Collision and Plateau Uplift, Institute of Tibetan Plateau Research, Chinese Academy of Sciences, Beijing, China, [2]CAS Center for Excellence in Tibetan Plateau Earth Sciences, Beijing, China, [3]Deutsches GeoForschungsZentrum GFZ, Telegrafenberg, Potsdam, Germany, [4]Earthquake Administration of Qianghai, Xining, China

Abstract We present detailed lithospheric images of the NE Tibetan Plateau by applying the depth migration technique to *S* receiver functions derived from 113 broadband stations. Our migrated images indicate that the lithosphere-asthenosphere boundary (LAB) lies at depths of 105–120 km beneath the Qilian terrane and reaches depths of 126–140 km below the Alxa and Ordos blocks. The most prominent variation in the LAB depth is the presence of LAB steps of no less than 20 km in the transition zone between the active NE Tibetan Plateau and the surrounding cratonic Alxa and Ordos blocks, which conflicts with the model of southward subduction of the Alxa and Ordos blocks. Furthermore, the marked LAB steps occur at 130 ± 10 km away from the southern surficial boundary faults between the NE Tibetan Plateau and the surrounding tectonic provinces, corresponding to the North Qilian fault and the Liupanshan fault, respectively. Therefore, we propose that these scenarios of LAB can be attributed to the delamination of fragmented mantle lithosphere in the transition zone between the NE Tibetan Plateau and the surrounding Alxa and Ordos blocks, triggered by lateral asthenospheric flow. In addition, our observations of a thin lithosphere with thickness of 107–115 km beneath the Songpan-Ganzi terrane and the west Qinlin orogen greatly facilitate the process of underlying lateral asthenospheric flow. The isostatic uplift of the plateau caused by the delamination of fragmented mantle lithosphere, together with increased horizontal compressive stress, may have led to the outward growth of the NE Tibetan Plateau.

1. Introduction

The northeastern (NE) Tibetan Plateau comprises the Songpan-Ganzi terrane (SPGZ), the Qaidam-Kunlun-West Qinling terrane (QKW), and the Qilian terrane (QL), which are divided by the Kunlun fault (KLF), the South Qilian suture (SQS)-West Qinling fault (WQL), and the North Qilian fault (NQF)-Haiyuan fault (HY)-Liupanshan fault (LPS), respectively (Figure 1; Meyer et al., 1998; Yin & Harrison, 2000). Changes in locations, ages, and styles of fault deformation suggest that the rate of deformation of the NE Tibetan Plateau has accelerated and that the orientation of crustal shortening has changed from NNE-SSW to NE-SW or ENE-WSW since 20–15 Ma (Duvall et al., 2013; Lease et al., 2011; D. Y. Yuan et al., 2013). Seismic reflection analysis, combined with other structural studies, reveals that the region of the NE Tibetan Plateau between the Kunlun fault and the Hexi Corridor (HC) has absorbed more than 250–350 km of Cenozoic N-S shortening (Zuza et al., 2016). In addition, the eastward exclusion of crustal material determined by the GPS measurements is accommodated by this shortening, occurring at rates of approximately 5.5 and 6.0 mm/year across the Qilian Shan and the Liupan Shan, respectively (P. Z. Zhang et al., 2004). These structural features indicate that the NE Tibetan Plateau is located at the leading edge of the northeastward expansion of the Tibetan Plateau, driven by continuous convergence following the collision of India and Eurasia.

To unravel the mechanisms controlling the shortening and outward growth of the NE Tibetan Plateau, numerous investigations have been carried out to delineate the structure of the crust and upper mantle using *P* and *S* wave receiver functions (*P*-RFs and *S*-RFs; e.g., X. Z. Shen, Yuan & Liu, 2015; X. Z. Shen et al., 2017; W. Wang, Wu, et al., 2017; Ye et al., 2015), teleseismic *P* wave traveltime tomography (e.g., H. L. Guo et al., 2017; Lei & Zhao, 2016), ambient noise and surface wave tomography (e.g., L. Li et al., 2013; W. S. Shen et al.,
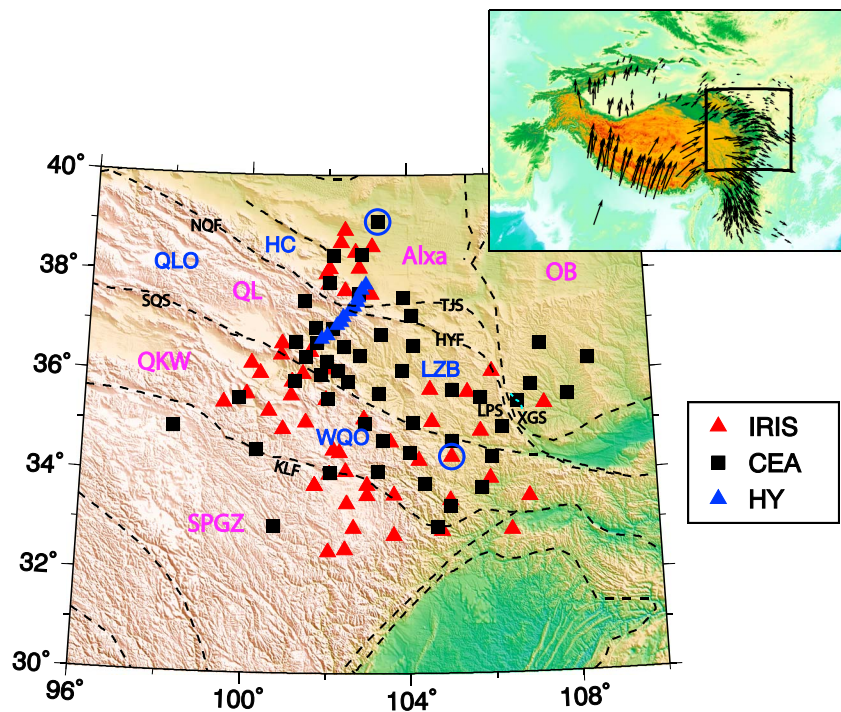
Figure 1. Topographic map showing the tectonic units of the northeastern Tibetan Plateau and the distribution of seismic stations employed in this study. The right top inset indicates the location of our study area (black box) and GPS velocities from P. Z. Zhang et al. (2004). The Incorporated Research Institutions for Seismology (IRIS) stations are denoted as red triangles, China Earthquake Administration (CEA) stations are black squares, and Haiyuan fault (HY) stations are blue triangles. The blue circles mark the locations of stations MIQ (black square) and GS07 (red triangle) shown in Figure 3. The geological provinces are as follows: SPGZ = Songpan-Ganzi terrane; QKW = Qaidam-Kunlun-West Qinling terrane; QL = Qilian terrane; Alxa = Alxa block; OB = Ordos block; QLO = Qilian orogen; LZB = Longzhong basin; WQO = west Qinling orogen; and HC = Hexi Corridor. The QL is further divided into the QLO in the west and LZB in the east. The WQO is located in the east of the QKW. The faults and suture are abbreviated as follows: KLF = Kunlun fault; SQS = south Qilian suture; NQF = North Qilian fault; HYF = Haiyuan fault; TJS = Tianjingshan fault; LPS = Liupanshan fault; XGS = Xiaoguanshan fault.

2016; Wei et al., 2017; Q. Zhang et al., 2011), and the shear wave splitting technique (e.g., Huang et al., 2017; Y. H. Li et al., 2011). However, the modes of lithospheric deformation and their connections to the northeastern expansion and growth of the NE Tibetan Plateau remain unresolved.

The southward subduction of the Asian lithospheric mantle, acting in multiple stages with inclined interfaces or over a long distance at a shallow angle, has been proposed to address the growth of the NE Tibetan Plateau (Tapponnier et al., 2001; Yin & Harrison, 2000). Seismic evidence for this subduction has been provided by the migrated *P*-RF and *S*-RF images beneath central and northern Tibet (Kind et al., 2002; Ye et al., 2015). However, several recent findings indicate that the Asian lithospheric mantle does not subduct beneath the NE Tibetan Plateau. A regional finite-frequency tomography study shows a rather homogenous low-velocity anomaly in the upper mantle beneath northern Tibet (Liang et al., 2012). Migrated *S*-RF images reveal that the NE Tibetan Plateau, which has a diffuse lithosphere-asthenosphere boundary (LAB), presents a thicker lithosphere than the adjacent Alxa and Ordos blocks (X. Z. Shen, Yuan & Liu, 2015; X. Z. Shen et al., 2017). The results of Rayleigh wave tomography reveal that no high velocities exist to the south of the Haiyuan fault, signifying the limited southward underthrusting of the North China Craton beneath the NE Tibetan Plateau (Wei et al., 2017). Furthermore, seismic anisotropy observations agree well with the model of the vertically coherent deformation between the crust and lithospheric mantle of the NE Tibetan Plateau (Chang et al., 2017; Q. Wang et al., 2016). Therefore, whether southward subduction of the Asian Plate is occurring beneath the NE Tibetan Plateau is still disputed.

The lower crustal flow model, developed by modeling the topographic gradients of swath profiles (Clark & Royden, 2000), points out that a branch of lower crustal flow exists between the Qaidam Basin and the
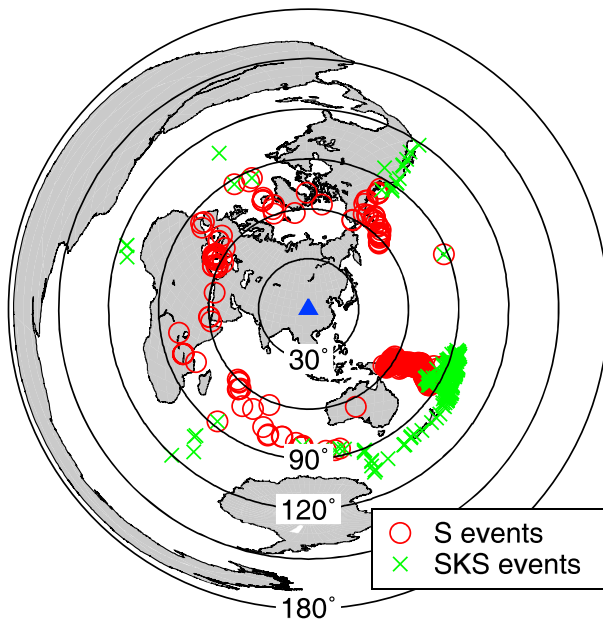
Figure 2. Map showing the epicentral distribution of *S* and *SKS* events used to calculate *S* wave receiver functions. The blue triangle represents the center of the study area.

Sichuan Basin. This hypothesis is supported by the presence of low-velocity lower crust with a NE trending fast direction of anisotropy (X. Z. Shen, Yuan & Ren, 2015). However, we also notice that these observed low-velocity zones mostly occur at depths of 20–40 km and are confined to the east Kunlun and west Qinling orogen (H. Y. Li et al., 2014; D. Zheng et al., 2016); thus, they do not satisfy the original definition of the lower crustal flow model. Furthermore, the absence of mafic lower crust and the low Poisson's ratios beneath the NE Tibetan Plateau as revealed by wide-angle seismic profiling and *P*-RFs argue against the development of lower crustal flow (X. Wang, Li, et al., 2017; Z. J. Zhang et al., 2013). In contrast, an asthenospheric flow model has been proposed, arguing that asthenospheric materials flow eastward through a low-velocity zone at depths of 125–200 km beneath the WQO (Q. Zhang et al., 2011). This asthenospheric flow model is also supported by the results of SKS wave splitting measurements, indicating that the large delay times with NW-SE fast polarization directions are continuous across the boundary of the NE Tibetan Plateau and the southwestern part of the Ordos block (Y. Yu & Chen, 2016) and a coupled crust-mantle deformation (Pandey et al., 2015). However, more seismic constraints are required to determine whether this model of asthenospheric flow below the NE Tibetan Plateau is correct.

In this study, we present high-resolution structural images of the LAB beneath the NE Tibetan Plateau and surrounding tectonic provinces obtained by the S-RF depth migration technique using waveforms from newly deployed stations together with other earlier experiments. The pronounced variations in LAB depth imaged in this study provide important clues to further understand the lithospheric deformation and expansion mechanism of the NE Tibetan Plateau.
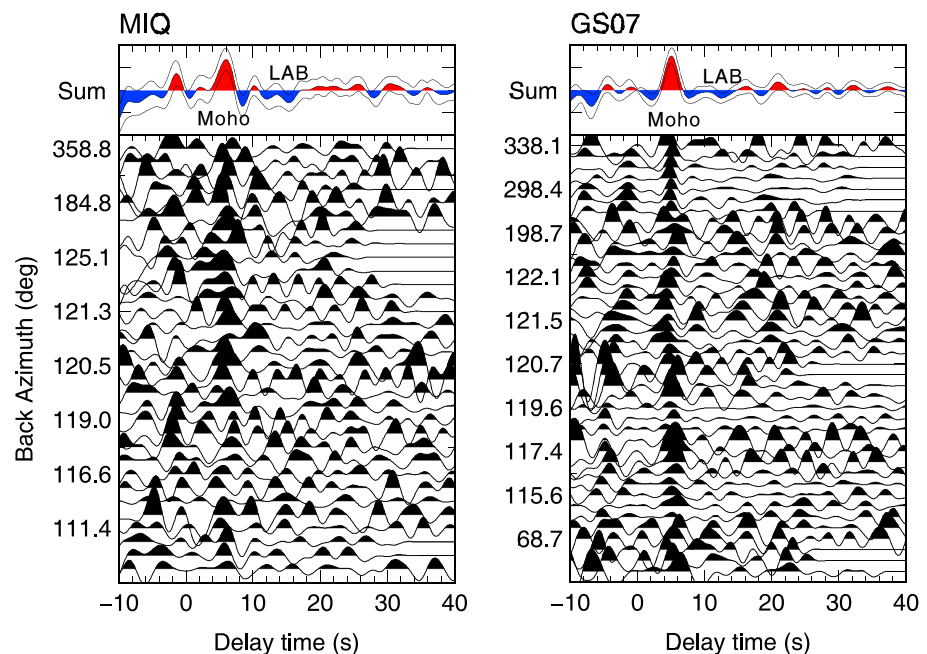
Figure 3. Individual *S* wave receiver functions with stacked traces for stations MIQ and GS07 denoted by the blue circles in Figure 1. Moveout-corrected *S* wave receiver functions are sorted by increasing back azimuths and filtered using a low-pass filter of 3 s. Two apparent phases in the sum traces are labeled Moho (red) and lithosphere-asthenosphere boundary (blue). The bootstrap uncertainties ($\pm 2\sigma$) are displayed on either side of the sum traces.
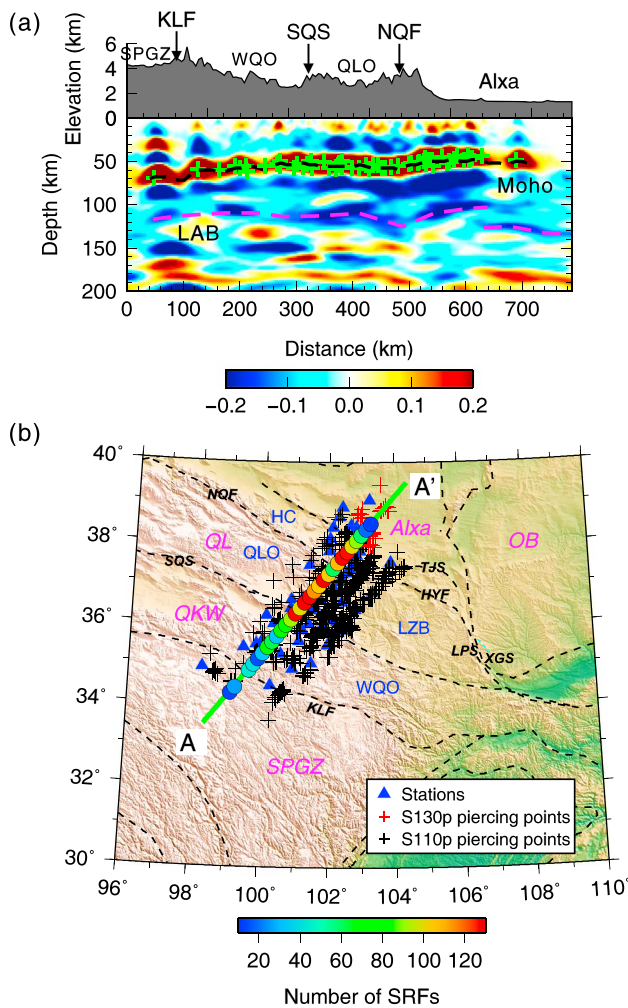
Figure 4. (a) Migrated image of *S* wave receiver functions along profile A-A′. For comparison, the measured Moho depths from Q. Wang et al. (2016; green crosses) are superimposed on our identified Moho conversions (black dashed line). The interpreted lithosphere-asthenosphere boundary (LAB) is shown as a pink dashed line. (b) Piercing points of *Sp* conversions at depths of 110 and 130 km are indicated using black and red crosses, respectively. The colored circles along profiles A–A′ show the number of *S* wave receiver functions within a moving distance of 20 km used for common conversion point stacking.

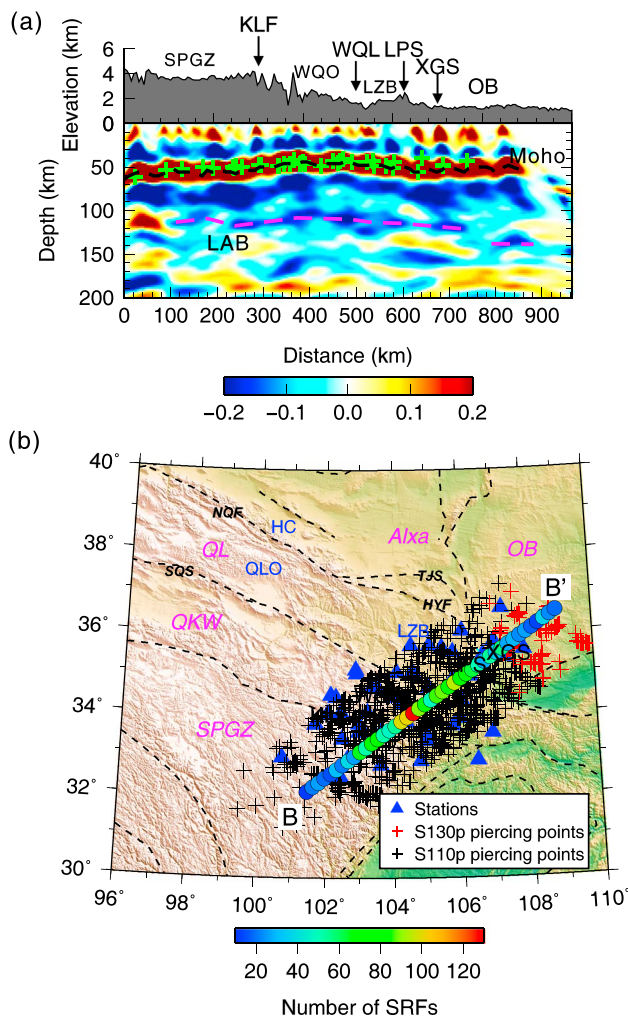## 2. Data and Methods

2.1. Data

The teleseismic waveform data used in this study were recorded by 113 broadband stations (Figure 1), including 48 permanent stations in Gansu and Qianghai Provinces from the China National Seismic Network of China Earthquake Administration, which recorded data from January 2009 to December 2010 (Data Management Centre of China National Seismic Network, 2007; X. F. Zheng et al., 2010), and 11 temporary stations of the HaiYuan array (HY), which were recently deployed by the Geophysical Group of the Institute of Tibetan Plateau Research, Chinese Academy of Sciences, from November 2014 to August 2016. The other 54 temporary stations were provided by the Incorporated Research Institutions for Seismology (IRIS), including 18 stations from the Gansu subarray of the ASCENT (X4) experiment (Q. Zhang et al., 2011), which was operated from January 2007 to December 2009, and 36 stations from the NETS array (ZV; L. Li et al., 2013, 2016), which collected data from January 2008 to December 2010. Furthermore, it is worth noting that the HY stations were designed to fill a large gap in the NETS array in order to ensure a more reasonable distribution of stations in our study area.

We utilize teleseismic events with magnitudes greater than 5.5 Mb and epicentral distances at 60°–85° and 85°–120° for *S* and *SKS* waves (*S* phases), respectively. After filtering with a zero-phase low-pass filter of 2 s, the extracted seismograms are visually inspected. Afterward, only those with high signal-to-noise ratios and clear onsets of *S* phases are selected for subsequent *S*-RF processing. The spatial distribution of these chosen earthquakes is shown in Figure 2.

2.2. *S*-RF Technique

The *S*-RF technique employs the *S*- and *SKS*-to-*P* (*Sp*) conversions to effectively determine the geometry of the LAB with a resolution higher than those provided by body wave and surface wave tomography. This method is more suitable for imaging the structural variations in the LAB than the *P*-RF method, because the *P*-to-*S* (*Ps*) conversions from the LAB are mostly contaminated by crustal reverberations (X. H. Yuan et al., 2006). In contrast, the *Sp* conversions arrive earlier than the direct *S* phases, so they are not disturbed by the multiple crustal reverberations that arrive after the *S* phases.

Following the processing procedures introduced by a review article (Kind et al., 2012), the calculation of the *S*-RFs mainly includes coordinate rotation and deconvolution. The three-component seismograms (*Z-N-E*) are rotated to the local ray coordinate system (P-SV-SH) using the back azimuth of and incidence angle. The back azimuth can be determined from the coordinates of the earthquake hypocenter and station location, while an optimal incidence angle is automatically chosen, with which the minimum amplitudes are realized within a time window of ±1 s for the *P* component at the arrival time of the *S* phases. The *P* component is deconvolved from the SV component to generate the *S*-RF. This deconvolution is performed using a spiking deconvolution method in the time domain. This deconvolution operator is strictly the inverse of the initial segment of the SV component that is obtained by minimizing the least squares differences between the observed seismogram and the desired delta-spike function. After deconvolution, the obtained *S*-RF is normalized to the maximum amplitude of the spike on the SV component. Finally, we also reverse the time axis and amplitudes of the *S*-RF to compare with those of the *P*-RF. In this case, a positive amplitude of *S*-RF represents a discontinuity in which velocity increases downward, while a negative amplitude denotes a velocity decrease with depth.

Figure 5. Same as Figure 4 but for profile B–B′.

To further intuitively depict the lateral variations in the lithospheric structure, we need to construct depth sections using a common conversion point (CCP) stacking approach (e.g., Dueker & Sheehan, 1997). In this method, each cross section is divided into grids, and each grid has a 2-km horizontal step and a 2-km vertical step. The *Sp* amplitudes of each *S*-RF are backprojected to their spatial locations where conversions occur along the incoming raypath. The raypaths of *S*-RFs at every station are determined using a modified IASP91 model in which crustal structure has been corrected by the available crustal thickness and *Vp/Vs* ratio (Q. Wang et al., 2016). Then, the amplitudes of all grids that are perpendicular to the profile within a width of 150 km are stacked along the designed profile to form the depth-migrated section. Finally, we apply the horizontal stacking within one Fresnel zone to generate a smoothed image for further tectonic analysis.

3. Results

The *S*-RFs for all the stations are obtained according to the methodology described above. Then, we manually pick the high-quality *S*-RFs at each station using the following criteria: (1) We removed *S*-RFs with unexpectedly large amplitudes or periodical oscillations compared with the stacked trace of all the *S*-RFs and (2) we selected *S*-RFs with clear Moho *Sp* phases appearing within ±1.5 s around the Moho *Ps* arrival time computed by the available crustal thickness and *Vp/Vs* ratio. After these selection procedures, 32% of the initial 6,412 *S*-RFs are rejected, and a total of 4,360 high-quality *S*-RFs from 657 events is retained for the study. Before further analysis, the retained *S*-RFs are filtered with a low-pass filter of 3 s. This filter can ensure a very reasonable trade-off between containing as many high frequencies as possible for the *S*-RFs and enhancing the coherence of phases in the migrated images. Figure 3 shows examples of the S-RFs for the stations MIQ (China Earthquake Administration) and GS07 (X4), which are located in the Alxa block and the WQO, respectively. For both stations, we stack the moveout-corrected S-RFs (with a reference slowness of 6.4 s per degree) and estimate the uncertainties of the stack traces using bootstrapping analysis. We repeat 500 bootstrap realizations, which are performed by stacking the same number of *S*-RFs that are randomly selected from the original *S*-RFs, and then compute two standard deviations (2σ) to determine the typical values of the uncertainties in the sum trace at each station. The most striking signal with the positive amplitude (in red) in the stacked traces related to the Moho appears at 6 s (54 km) at MIQ and 5.2 s (46 km) at GS07. A negative conversion (in blue) associated with the LAB arrives at 15.3 s (138 km) at MIQ and 12.3 s (110 km) at GS07. These features clearly indicate that the Alxa block has a thicker crust and lithosphere than the WQO.
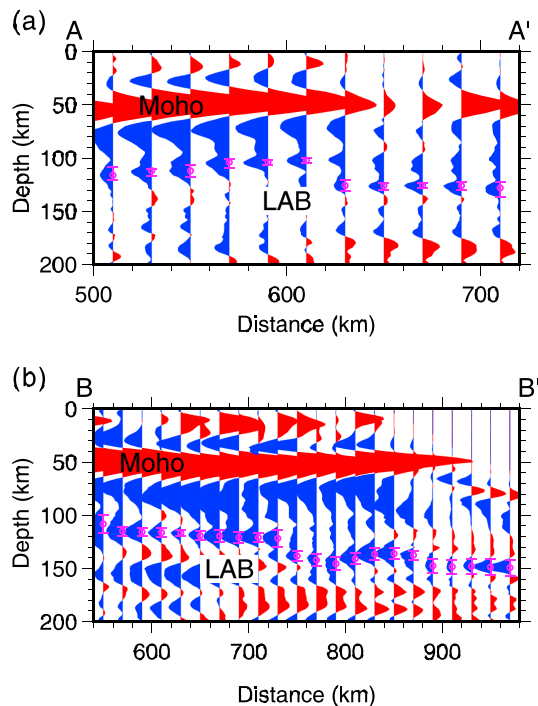
In Figures 4 and 5, we present the depth migrated images of the *S*-RFs along two NE-SW trending profiles A–A′ and B–B′. Both profiles with an E-W interval of 400 km traverse the eastern SPGZ and WQO. However, profile A–A′ reaches the Alxa block across the Qilian orogen (QLO) and the NQF, and profile B–B′ extends to the Ordos block through the Longzhong Basin (LZB) and the LPS, given that the QL consists of the QLO in the west and LZB in the east.

As the most prominent discontinuity, the Moho is clearly observed at depths of 40–70 km along both profiles (Figures 4 and 5). Compared with the Moho depths that are reliably estimated using the modified H-κ stacking method of the *P*-RFs (Q. Wang et al., 2016), we find that the average difference in the Moho depth is 4.5 km, indicating a reasonable consistency between these two results obtained using two independent methods, which also demonstrates the accuracy of our migrated *S*-RF images. Because the *S*-RFs are characterized by lower frequencies than P-RFs, we focus here on discussing the variations in LAB depth rather than crustal structure.

Figure 6. Illustration of the wiggles of the stacked traces across the transition zone from the Tibetan Plateau to the surrounding Alxa and Ordos blocks along profiles (a) A–A′ and (b) B–B′. The pink circles and bars mark the identified depths of lithosphere-asthenosphere boundary (LAB) with their two standard deviations.

Strong negative phases immediately below the Moho are seen along both profiles and are probably side lobes of the Moho *Sp* conversions. In addition, deeper negative conversions at depths of 102–150 km can be steadily traced along both profiles. We interpret this phase as the *Sp* conversion of the LAB, which determines the thickness of the lithosphere. Along profile A–A′ (Figure 4), the LAB slowly shallows northward from 112 ± 6 km beneath the northern SPGZ to 107 ± 4 km below the WQO. It then deepens to 121 ± 6 km under the NQF and rises to 102 ± 4 km beneath the southern Alxa block, forming a concave shape across a distance of 200 km. The depth of the LAB further to the north, with a step of 24 km, abruptly deepens to 126 ± 5 km beneath the Alxa block. For profile B–B′ (Figure 5), the depth of the LAB decreases slightly from 115 ± 4 km beneath the SPGZ to 104 ± 5 km under the WQO, and it reaches 120 ± 5 km beneath the southwestern Ordos block. Similarly, the LAB shows a step of 20 km over a lateral distance of 100 km and lies at a depth of 140 ± 5 km beneath the northern end of this profile. In addition, we also present another two depth-migrated S-RF images along profiles C-C′ and D-D′ (Figures S1 and S2 in the supporting information). It is clear that the estimated LAB depths beneath the same sampled region roughly coincide with those observations derived from the images along profiles A–A′ and B–B′.

To further explore the reliability of the LAB steps, we plot the wiggles of the stacked traces across the transition zone from the NE Tibetan plateau to the surrounding Alxa and Ordos blocks along profiles A–A′ and B–B′. These stacked traces are generated by summing the CCP stacking grids within a moving window of 20 km along each profile (Figure 6). It is apparent that the LAB conversions are clearly visible and can be continuously traced along each profile. The prominent finding of this study is the existence of the LAB step, indicating the distinct change in the LAB depth, which is located at a distance of 620 ± 10 km along profile A–A′ and 740 ± 10 km along profile B–B′.

4. Discussion

4.1. Stability Analysis of the Migrated Images

The stability of the identified LAB for each profile is evaluated using the bootstrap technique. For each bootstrap process, we randomly select 63% of all the *S*-RFs and then duplicate about 60% of the chosen ones so that the total number of *S*-RFs remains the same as that for the original data set along each section (Liu et al., 2003). We perform 500 bootstrapping realizations of CCP stacking, and the standard deviation in each grid is calculated based on the 500 migrated images obtained along the chosen four profiles (supporting information Figures S3–S6). We consider grids with amplitudes of more than 1.5 standard deviations to represent reliable observations for the following structural interpretations. Other strong negative patches below the LAB are likely noise or scattered energy related to local structural heterogeneities in the upper mantle. Although the distribution of piercing points at LAB depths (Figures 4 and 5 and supporting information Figures S1 and S2) and the raypaths along the four profiles (supporting information Figures S3–S6) show uneven ray coverage, the imaged LAB is sufficiently sampled by the raypaths. In particular, we find that no path gap corresponds to the identified LAB steps.

The selected reference model involved in the ray tracing technique can introduce errors in the depth estimates of subsurface discontinuities. As demonstrated in previous studies (e.g., L. Chen, 2009; L. Chen et al., 2008; Xu et al., 2017), the depth errors introduced by a 5% velocity difference from the reference model are 3 km for the Moho at a depth of 60 km and 5 km for the LAB at a depth of 120 km. The uncertainty associated with the well-resolved LAB in the migrated image is smaller than the vertical resolution of the S-RFs at the depth of the LAB (9 km). Therefore, the choice of velocity model does not significantly affect the appearance of the migrated images.
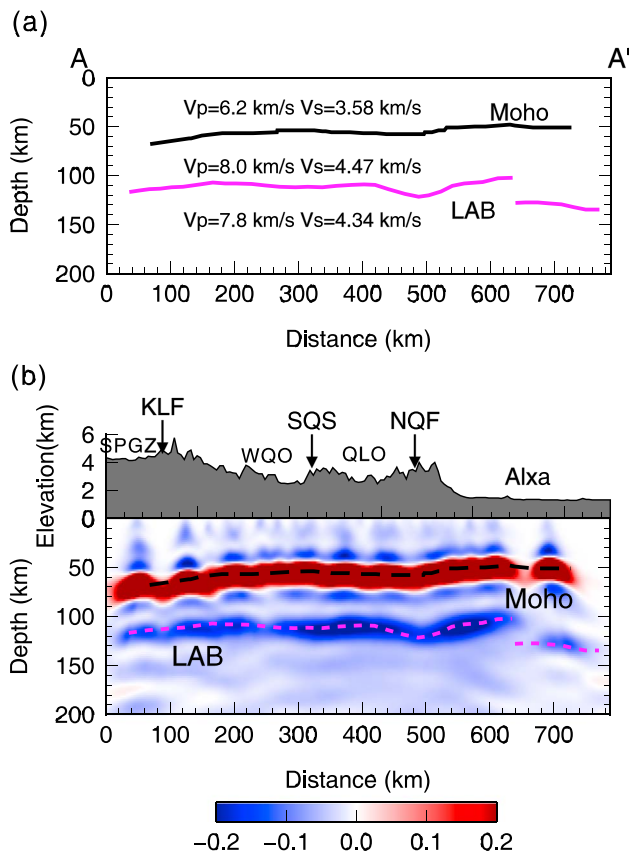
Figure 7. (a) Forward velocity model designed with the depths of Moho and lithosphere-asthenosphere boundary (LAB) delineated from the observed image (Figure 4a) for profile A–A′. (b) Migrated image of the noisy S wave receiver functions based on the real data coverage of profile A–A′. Black and pink dashed lines give the estimated depths of the Moho and LAB along profile A–A′, respectively.

4.2. Synthetic Tests

To assess the anisotropy effects on the observed LAB, we carry out a synthetic test using a 1-D isotropic model with an additional anisotropic layer (supporting information Figure S7a). This model consists of the following: (1) a 50-km-thick crust ($Vp = 6.2$ km/s, $Vs = 3.58$ km/s, density $\rho = 2,754$ kg/m^3), (2) a 70-km-thick mantle lid ($Vp = 8.0$ km/s, $Vs = 4.50$ km/s, density $\rho = 3,343$ kg/m^3), and (3) a mantle half-space ($Vp = 7.8$ km/s, $Vs = 4.10$ km/s, density $\rho = 3,132$ kg/m^3). An anisotropic layer with a 30-km thickness and 10% S anisotropy is placed at the base of the lithosphere. We apply the RAYSUM package to calculate the synthetic S-RFs (Frederiksen & Bostock, 2000). The amplitudes of the LAB phases in the resultant S-RFs show periodical variations with back azimuth, while the depths of the LAB exhibit almost no change (supporting information Figure S7b). Thus, anisotropy has a negligible influence on the estimated LAB depths.

To further demonstrate the robust features of the imaged LAB, we perform resolution tests of the S-RFs by forward modeling. We design the forward models based on the observed Moho and LAB depths shown in Figures 4 and 5, as well as other model parameters as described before (Figures 7a and 8a). To make the synthetics S-RFs represent the real Earth environment as closely as possible, we create noisy S-RFs by adding random noises to the synthetic S-RFs. Figure S7 given in the supporting information shows the comparison between a noisy S-RF and a synthetic S-RF. The depth-migrated images using these noisy S-RFs are created in the same way as those using the real data from profiles A–A′ and B–B′ (Figures 7b and 8b). These restored migration images can well resolve the structural features of the LAB as displayed in the real data images, especially the existence of both LAB steps. However, the recovered LAB steps occur over a lateral distance of 60 ± 10 km, which are comparable to the previous analysis of the lateral resolution of the LAB images, indicating that a 40-km step in the LAB occurring over no more than 100 km can be reliability detected (L. Chen, 2009; L. Chen et al., 2008). In addition, synthetic waveforms computed from the spectral element method produce the pronounced duplexing of Sp conversions across a steep sloped LAB (Lekic & Fischer, 2017). This feature of the duplexing is clearly observed in the CCP stacking images along profiles A-A′ and B-B′ (Figure 6), but they are not well resolved in our modeling results. This discrepancy in the synthetic tests is probably associated with the application of the more sophisticated spectral element method and inadequate data coverage. However, our synthetic tests are capable of confirming the reliability of the interpreted tectonic features.

4.3. LAB Beneath the NE Tibetan Plateau

The LAB identified in our migrated S-RF images indicate that the lithospheric thicknesses of the SPGZ and WQO range from 107 to 115 km (Figures 4 and 5), compatible with the results of the surface wave inversion indicating that the lithosphere is 90–100 km thick (L. Li et al., 2013, 2016). Our observations indicating that the LAB is located at an average depth of 111 ± 4 km are in good agreement with the estimate of 110 ± 10 km determined from the stacking traces of S-RFs within a bin of 1° × 1° to the east of profile B-B′ (Hu et al., 2011). Evidence from mantle xenoliths suggests that the stratified lithosphere of the WQO is located at an estimated depth of 120 km (Su et al., 2010).

The imaged LAB at depths of 105–121 km beneath the QL is supported by the analysis of the stacked S-RFs, which demonstrates that the LAB beneath the QL is present at 12–14 s (i.e., depths of 105–125 km; Feng et al., 2014). The single stacked trace of all the S-RFs within the QL also indicates that the negative signal from the LAB is observed at 11 s (100 km; X. Z. Shen, Yuan & Liu, 2015), which is comparable with our observations.
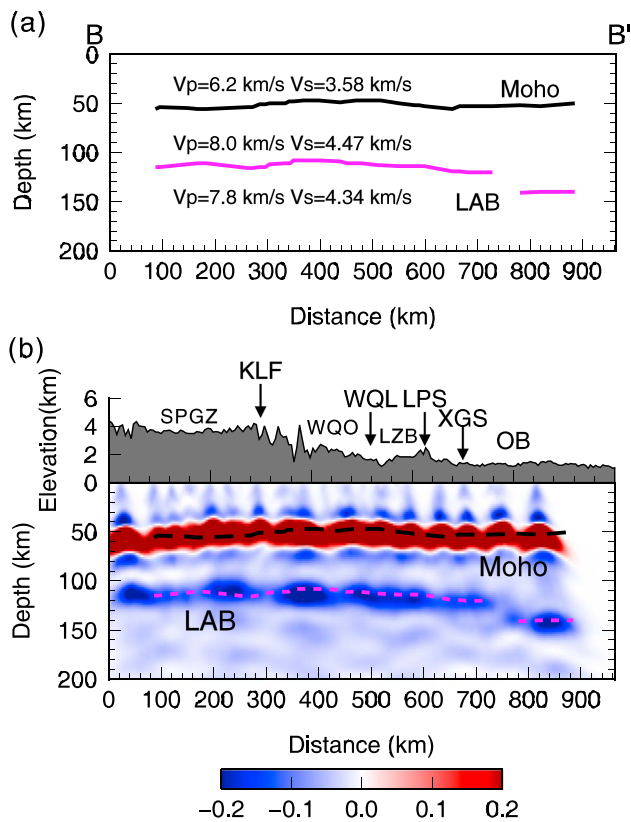
Figure 8. Same as Figure 7 but for profile B-B′.

The *Sp* conversions of the LAB across the KLF are weaker along profile A–A′ than those along profile B–B′, which is probably due to that the former LAB is characterized by a broader gradient. This feature is also supported by the presence of one strong low-velocity anomaly at a depth of 120 km in almost the same place, resulted from local asthenospheric upwelling (L. Li et al., 2013).

4.4. Lab Under the Alxa and Ordos Blocks

Below Moho depth, we image a coherent negative signal at depths of 126–140 km beneath the Alxa and Ordos blocks. In oceanic and tectonically active regions, this negative *Sp* phase is interpreted as the LAB (e.g., Fischer et al., 2010; Kind et al., 2012). However, this negative *Sp* signal is also likely to represent a midlithospheric discontinuity (MLD) in cratonic areas, as previously interpreted in North America and Australia, with a wide variety of possible causes (e.g., thermal gradient, composition, and anisotropy; e.g., Abt et al., 2010; Ford et al., 2010; Selway et al., 2015). In this study, we prefer to interpret it as the LAB rather than a MLD on the basis of previous observations by the surface wave tomography and *S*-RF techniques. The most recently constructed 3-D shear wave velocity model places the LAB depth at 125 ± 5 km close to the northern end of profile B–B′ (S. L. Li et al., 2018), which is in good agreement with our interpreted LAB. Meanwhile, our observations are also supported by another independent shear wave velocity model indicating that the lithospheric thickness beneath the Ordos and SW Alxa blocks is 100–140 km (Y. Li et al., 2017). Across the northern part of profile B–B′, a MLD interpreted as an ancient and mechanistically weak zone within the lithospheric mantle is observed at depths of 80–100 km beneath southern Ordos, which is significantly shallower than our estimated LAB (L. Chen et al., 2014). In contrast, the imaged LAB using *S*-RFs abruptly shallows from 135 ± 5 km under the western border of the Ordos block to 105 ± 5 km within the LZB (L. Chen et al., 2014), which also supports our interpretation.

4.5. Implications for the Presence of LAB Steps

The pronounced features in our findings are the existence of LAB steps of no less than 20 km along the two profiles. Given that subduction usually corresponds to a dipping LAB, we suggest that the surrounding Alxa and Ordos blocks do not subduct southward beneath the eastern part of the QL. This interpretation is supported by recent tomographic images displaying obvious low-velocity anomalies dominating the NE Tibetan Plateau above a depth of 200 km (H. L. Guo et al., 2017). The recent 3-D shear wave velocity models from teleseismic Rayleigh wave tomography illustrate that no high-velocity materials can be continuously traced beneath the NE Tibetan Plateau (Wei et al., 2017), in good agreement with our interpretation. Furthermore, more evidence for this inference is provided by the results of regional finite-frequency tomography (e.g., Liang et al., 2012), S-RF analysis (e.g., X. Z. Shen, Yuan & Liu, 2015; X. Z. Shen et al., 2017), and seismic anisotropy observations (e.g., Chang et al., 2017; Q. Wang et al., 2016), as discussed in detail in section 1.

The LAB steps, regarded as lithospheric boundaries, occur at 130 ± 10 km away from the southern surficial boundary faults between the NE Tibetan Plateau and the surrounding Alxa and Ordos blocks, corresponding to the NQF and the LPS, respectively. We propose that these scenarios of LAB can result from the delamination of fragmented mantle lithosphere in the transition zone between the NE Tibetan Plateau and the surrounding Alxa and Ordos blocks, and the influx of hot Tibetan asthenospheric materials transferred through the asthenospheric flow driven by northward underthrusting of the Indian plate (Figure 9). A similar structure
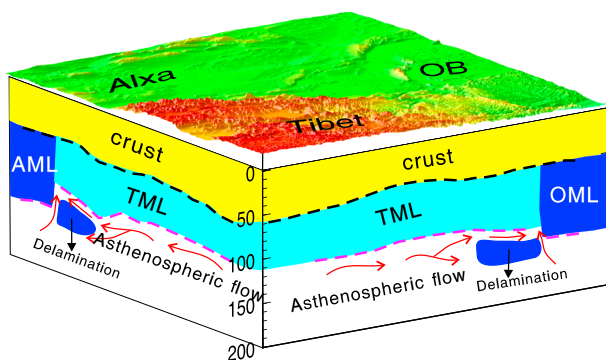
Figure 9. Schematic illustrations of our observations with their corresponding tectonic interpretations. The identified Moho and lithosphere-asthenosphere boundary are marked by black and red dashed lines, respectively. AML = Alxa mantle lithosphere; OML = Ordos mantle lithosphere; TML = Tibetan mantle lithosphere.

has been reported in the transition zone from the North American Craton to the Cordillera Plateau, where a Rayleigh wave tomography model shows the existence of a marked step change in lithospheric thickness, implying the occurrence of large-scale delamination of the lithosphere triggered by the upwelling of mantle material (Bao et al., 2014).

This asthenospheric flow probably originates from northern Tibet, including the northern Qiangtang terrane and the western SPGZ, which are compatible with the locations of the strong low-velocity anomalies heated by asthenospheric upwelling (M. Chen et al., 2017), as well as the zones of *Pn* low velocity and *Sn* high attenuation (Barazangi & Ni, 1982). Moreover, the observed thinner lithosphere below the SPGZ and the WQO can greatly facilitate this flow. The spatial and temporal distribution of Cenozoic potassic magmatism (X. H. Yu et al., 2009) and the NE bulge in the low-gravity anomalies (Bi et al., 2016) also favor the existence of lateral asthenospheric flow beneath the NE Tibetan Plateau. The continuity of the long delay times, as well as the NW-SE fast polarization directions across the southwestern boundary of the Ordos block, can be well explained by the presence of lateral asthenospheric flow (Y. Yu & Chen, 2016). Beneath the WQO, the measured lower layer delay times of 1.0–1.5 s are likely produced by the asthenospheric flow except for the deformation in mantle lithosphere (Huang et al., 2017). Furthermore, the most recent results from surface wave tomography show an interconnected low-velocity zone at depths of 100–200 km under the northern Ordos block and its surrounding regions, suggesting that the asthenosphere beneath the NE Tibetan Plateau flows northeast toward the northern Ordos lithosphere (S. L. Li et al., 2018).

The delamination of fragmented mantle lithosphere and the influx of hotter asthenosphere not only reduce the load of the overlying lithosphere but also cause isostatic uplift of the plateau. This isostatic uplift together with the increased horizontal compressive stress may have led to the outward growth of the NE Tibetan Plateau (Molnar et al., 1993). D. Y. Yuan et al. (2013) summarizes that the acceleration of deformation and the northward migration of fault activity, including the formation of new faults, have occurred since approximately 20 Ma (supporting information Figure S8). The superposition of the Moho observed from the stacking profiles of the *P*-RFs represents strong evidence that the Tianjinshan fault (TJS) has replaced the Haiyuan fault (HY) as the growth front of the NE Tibetan Plateau (X. Z. Shen et al., 2017). The crustal architecture across the Tibet-Ordos transition zone, constrained by the deep seismic reflection image, regional aeromagnetic anomalies, and surface geology, indicates that the XiaoguanShan fault (XGS) to the east of the LPS marks the easternmost edge of the northeastern growth of the Tibetan Plateau (X. Y. Guo et al., 2015).

5. Conclusions

This study presents high-resolution lithospheric structural images beneath the NE Tibetan Plateau and its surrounding blocks by employing the depth migration technique to *S*-RFs derived from 113 broadband stations. The main findings of this study, along with their respective structural interpretations, are summarized as follows:

1. The most pronounced features in the imaged LAB depths are the presence of LAB steps of no less than 20 km along the two NE-SW trending profiles. These steps significantly separate the thinner lithosphere of the QL with LAB depths of 105–120 km from the thicker lithosphere beneath the Alxa and Ordos blocks with LAB depths of 126–140 km. This observation challenges the model of southward subduction of the Alxa and Ordos blocks beneath the eastern part of the QL.
2. The LAB steps are found at 130 ± 10 km away from the southern boundary faults at the surface between the NE Tibetan Plateau and the surrounding Alxa and Ordos blocks, corresponding to the NQF and the LPS, respectively. Therefore, we interpret this observation, together with the presence of LAB steps, as the result of the delamination of fragmented mantle lithosphere in the transition zone between the NE Tibetan Plateau and the surrounding Alxa and Ordos blocks, and the influx of hot Tibetan asthenospheric materials originating from asthenospheric flow.
3. Our migrated images reveal a thin lithosphere with thickness of 107–115 km beneath the SPGZ and the WQO, which dramatically facilitates the process of lateral asthenospheric flow.
4. The isostatic uplift of the plateau resulted from the delamination of fragmented mantle lithosphere, together with the increased horizontal compressive stress, may account for the outward growth of the NE Tibetan Plateau.

References

Abt, D. L., Fischer, K. M., French, S. W., Ford, H. A., Yuan, H. Y., & Romanowicz, B. (2010). North American lithospheric discontinuity structure imaged by Ps and Sp receiver functions. *Journal of Geophysical Research*, *115*, B09301. https://doi.org/10.1029/2009JB006914

Bao, X. W., Eaton, D. W., & Guest, B. (2014). Plateau uplift in western Canada caused by lithospheric delamination along a craton edge. *Nature Geoscience*, *7*(11), 830–833. https://doi.org/10.1038/NGEO2270

Barazangi, M., & Ni, J. (1982). Velocities and propagation characteristics of Pn and Sn beneath the Himalayan Arc and Tibetan Plateau—Possible evidence for underthrusting of Indian continental lithosphere beneath Tibet. *Geology*, *10*(4), 179–185. https://doi.org/10.1130/0091-7613

Bi, B. T., Hu, X. Y., Li, L. Q., Zhang, H. L., Liu, S., & Cai, J. C. (2016). Multi-scale analysis to the gravity field of the northeastern Tibetan plateau and its geodynamic implications. *Chinese Journal of Geophysics-Chinese Edition*, *59*(2), 543–555. https://doi.org/10.6038/cjg20160213

Chang, L. J., Ding, Z. F., Wang, C. Y., & Flesch, L. M. (2017). Vertical coherence of deformation in lithosphere in the NE margin of the Tibetan plateau using GPS and shear-wave splitting data. *Tectonophysics*, *699*, 93–101. https://doi.org/10.1016/j.tecto.2017.01.025

Chen, L. (2009). Lithospheric structure variations between the eastern and central North China Craton from S- and P-receiver function migration. *Physics of the Earth and Planetary Interiors*, *173*(3–4), 216–227. https://doi.org/10.1016/j.pepi.2008.11.011

Chen, L., Jiang, M. M., Yang, J. H., Wei, Z. G., Liu, C. Z., & Ling, Y. (2014). Presence of an intralithospheric discontinuity in the central and western North China Craton: Implications for destruction of the craton. *Geology*, *42*(3), 223–226. https://doi.org/10.1130/G35010.1

Chen, L., Tao, W., Zhao, L., & Zheng, T. Y. (2008). Distinct lateral variation of lithospheric thickness in the northeastern North China Craton. *Earth and Planetary Science Letters*, *267*(1–2), 56–68. https://doi.org/10.1016/j.epsl.2007.11.024

Chen, M., Niu, F., Tromp, J., Lenardic, A., Lee, C.-T. A., & Cao, W. (2017). Lithospheric foundering and underthrusting imaged beneath Tibet. *Nature Communications*, *8*, 15659. https://doi.org/10.1038/ncomms15659

Clark, M. K., & Royden, L. H. (2000). Topographic ooze: Building the eastern margin of Tibet by lower crustal flow. *Geology*, *28*(8), 703–706. https://doi.org/10.1130/0091-7613(2000)28<703:Tobtem>2.0.Co;2

Data Management Centre of China National Seismic Network (2007). Waveform data of China National Seismic Network. *Institute of Geophysics, China Earthquake Administration*, https://doi.org/10.11998/SeisDmc/SN, http://www.seisdmc.ac.cn

Dueker, K. G., & Sheehan, A. F. (1997). Mantle discontinuity structure from midpoint stacks of converted P to S waves across the Yellowstone hotspot track. *Journal of Geophysical Research*, *102*(B4), 8313–8327. https://doi.org/10.1029/96JB03857

Duvall, A. R., Clark, M. K., Kirby, E., Farley, K. A., Craddock, W. H., & Li, C. Y. (2013). Low-temperature thermochronometry along the Kunlun and Haiyuan Faults, NE Tibetan Plateau: Evidence for kinematic change during late-stage orogenesis. *Tectonics*, *32*, 1190–1211. https://doi.org/10.1002/tect.20072

Feng, M., Kumar, P., Mechie, J., Zhao, W., Kind, R., & Su, H. (2014). Structure of the crust and mantle down to 700 km depth beneath the East Qaidam basin and Qilian Shan from P and S receiver functions. *Geophysical Journal International*, *199*(3), 1416–1429. https://doi.org/10.1093/gji/ggu335

Fischer, K. M., Ford, H. A., Abt, D. L., & Rychert, C. A. (2010). The lithosphere-asthenosphere boundary. *Annual Review of Earth and Planetary Sciences*, *38*(1), 551–575. https://doi.org/10.1146/annurev-earth-040809-152438

Ford, H. A., Fischer, K. M., Abt, D. L., Rychert, C. A., & Elkins-Tanton, L. T. (2010). The lithosphere-asthenosphere boundary and cratonic lithospheric layering beneath Australia from Sp wave imaging. *Earth and Planetary Science Letters*, *300*(3–4), 299–310. https://doi.org/10.1016/j.epsl.2010.10.007

Frederiksen, A. W., & Bostock, M. G. (2000). Modelling teleseismic waves in dipping anisotropic structures. *Geophysical Journal International*, *141*(2), 401–412. https://doi.org/10.1046/j.1365-246x.2000.00090.x

Guo, H. L., Ding, Z. F., & Xu, X. M. (2017). Upper mantle structure beneath the northern south-north seismic zone from teleseismic traveltime data. *Chinese Journal of Geophysics-Chinese Edition*, *60*(1), 86–97. https://doi.org/10.6038/cjg20170108

Guo, X. Y., Gao, R., Wang, H. Y., Li, W. H., Keller, G. R., & Xu, X. (2015). Crustal architecture beneath the Tibet-Ordos transition zone, NE Tibet, and the implications for plateau expansion. *Geophysical Research Letters*, *42*, 10,631–10,639. https://doi.org/10.1002/2015GL066668

Hu, J. F., Xu, X. Q., Yang, H. Y., Wen, L. M., & Li, G. Q. (2011). S receiver function analysis of the crustal and lithospheric structures beneath eastern Tibet. *Earth and Planetary Science Letters*, *306*(1–2), 77–85. https://doi.org/10.1016/j.epsl.2011.03.034

Huang, Z. C., Tilmann, F., Xu, M. J., Wang, L. S., Ding, Z. F., & Mi, N. (2017). Insight into NE Tibetan Plateau expansion from crustal and upper mantle anisotropy revealed by shear-wave splitting. *Earth and Planetary Science Letters*, *478*, 66–75. https://doi.org/10.1016/j.epsl.2017.08.030

Kind, R., Yuan, X., Saul, J., Nelson, D., Sobolev, S. V., & Mechie, J. (2002). Seismic images of crust and upper mantle beneath Tibet: Evidence for Eurasian plate subduction. *Science*, *298*(5596), 1219–1221. https://doi.org/10.1126/science.1078115

Kind, R., Yuan, X. H., & Kumar, P. (2012). Seismic receiver functions and the lithosphere-asthenosphere boundary. *Tectonophysics*, *536-537*, 25–43. https://doi.org/10.1016/j.tecto.2012.03.005

Lease, R. O., Burbank, D. W., Clark, M. K., Farley, K. A., Zheng, D. W., & Zhang, H. P. (2011). Middle Miocene reorganization of deformation along the northeastern Tibetan Plateau. *Geology*, *39*(4), 359–362. https://doi.org/10.1130/G31356.1

Lei, J. S., & Zhao, D. P. (2016). Teleseismic P-wave tomography and mantle dynamics beneath eastern Tibet. *Geochemistry, Geophysics, Geosystems*, *17*, 1861–1884. https://doi.org/10.1002/2016GC006262

Lekic, V., & Fischer, K. M. (2017). Interpreting spatially stacked Sp receiver functions. *Geophysical Journal International*, *210*(2), 874–886. https://doi.org/10.1093/gji/ggx206

Li, H. Y., Shen, Y., Huang, Z. X., Li, X. F., Gong, M., & Shi, D. A. (2014). The distribution of the mid-to-lower crustal low-velocity zone beneath the northeastern Tibetan Plateau revealed from ambient noise tomography. *Journal of Geophysical Research: Solid Earth*, *119*, 1954–1970. https://doi.org/10.1002/2013JB010374

Li, L., Li, A. B., Murphy, M. A., & Fu, Y. Y. V. (2016). Radial anisotropy beneath northeast Tibet, implications for lithosphere deformation at a restraining bend in the Kunlun fault and its vicinity. *Geochemistry, Geophysics, Geosystems*, *17*, 3674–3690. https://doi.org/10.1002/2016GC006366

Li, L., Li, A. B., Shen, Y., Sandvol, E. A., Shi, D. N., & Li, H. Y. (2013). Shear wave structure in the northeastern Tibetan Plateau from Rayleigh wave tomography. *Journal of Geophysical Research: Solid Earth*, *118*, 4170–4183. https://doi.org/10.1002/jgrb.50292

Li, S. L., Guo, Z., Chen, Y., Yang, Y. J., & Huang, Q. H. (2018). Lithospheric structure of the Northern Ordos from ambient noise and teleseismic surface wave tomography. *Journal of Geophysical Research: Solid Earth*, *123*, 6940–6957. https://doi.org/10.1029/2017JB015256

Li, Y., Pan, J., Wu, Q., & Ding, Z. (2017). Lithospheric structure beneath the northeastern Tibetan Plateau and the western Sino-Korea Craton revealed by Rayleigh wave tomography. *Geophysical Journal International*, *210*(2), 570–584. https://doi.org/10.1093/gji/ggx181

Li, Y. H., Wu, Q. J., Zhang, F. X., Feng, Q. Q., & Zhang, R. Q. (2011). Seismic anisotropy of the northeastern Tibetan Plateau from shear wave splitting analysis. *Earth and Planetary Science Letters*, *304*(1–2), 147–157. https://doi.org/10.1016/j.epsl.2011.01.026

Liang, X. F., Sandvol, E., Chen, Y. J., Hearn, T., Ni, J., & Klemperer, S. (2012). A complex Tibetan upper mantle: A fragmented Indian slab and no south-verging subduction of Eurasian lithosphere. *Earth and Planetary Science Letters*, *333-334*, 101–111. https://doi.org/10.1016/j.epsl.2012.03.036

Liu, K. H., Gao, S. S., Silver, P. G., & Zhang, Y. K. (2003). Mantle layering across central South America. *Journal of Geophysical Research*, *108*(B11), 2510. https://doi.org/10.1029/2002JB002208

Meyer, B., Tapponnier, P., Bourjot, L., Metivier, F., Gaudemer, Y., & Peltzer, G. (1998). Crustal thickening in Gansu-Qinghai, lithospheric mantle subduction, and oblique, strike-slip controlled growth of the Tibet plateau. *Geophysical Journal International*, *135*(1), 1–47. https://doi.org/10.1046/j.1365-246X.1998.00567.x

Molnar, P., England, P., & Martinod, J. (1993). Mantle dynamics, uplift of the Tibetan Plateau, and the Indian monsoon. *Reviews of Geophysics*, *31*(4), 357–396. https://doi.org/10.1029/93RG02030

Pandey, S., Yuan, X. H., Debayle, E., Tilmann, F., Priestley, K., & Li, X. Q. (2015). Depth-variant azimuthal anisotropy in Tibet revealed by surface wave tomography. *Geophysical Research Letters*, *42*, 4326–4334. https://doi.org/10.1002/2015GL063921

Selway, K., Ford, H., & Kelemen, P. (2015). The seismic mid-lithosphere discontinuity. *Earth and Planetary Science Letters*, *414*, 45–57. https://doi.org/10.1016/j.epsl.2014.12.029

Shen, W. S., Ritzwoller, M. H., Kang, D., Kim, Y., Lin, F. C., & Ning, J. Y. (2016). A seismic reference model for the crust and uppermost mantle beneath China from surface wave dispersion. *Geophysical Journal International*, *206*(2), 954–979. https://doi.org/10.1093/gji/ggw175

Shen, X. Z., Liu, M., Gao, Y., Wang, W. J., Shi, Y. T., & An, M. J. (2017). Lithospheric structure across the northeastern margin plateau: Implications for the plateau's lateral growth. *Earth and Planetary Science Letters*, *459*, 80–92. https://doi.org/10.1016/j.epsl.2016.11.027

Shen, X. Z., Yuan, X. H., & Liu, M. (2015). Is the Asian lithosphere underthrusting beneath northeastern Tibetan Plateau? Insights from seismic receiver functions. *Earth and Planetary Science Letters*, *428*, 172–180. https://doi.org/10.1016/j.epsl.2015.07.041

Shen, X. Z., Yuan, X. H., & Ren, J. S. (2015). Anisotropic low-velocity lower crust beneath the northeastern margin of Tibetan Plateau: Evidence for crustal channel flow. *Geochemistry, Geophysics, Geosystems*, *16*, 4223–4236. https://doi.org/10.1002/2015GC005952

Stammler, K. (1993). Seismichandler programmable multichannel data handler for interactive and automatic processing of seismological analyses. *Computers & Geosciences*, *19*(2), 135–140. https://doi.org/10.1016/0098-3004(93)90110-Q

Su, B. X., Zhang, H. F., Sakyi, P. A., Ying, J. F., Tang, Y. J., & Yang, Y. H. (2010). Compositionally stratified lithosphere and carbonatite metasomatism recorded in mantle xenoliths from the Western Qinling (Central China). *Lithos*, *116*(1–2), 111–128. https://doi.org/10.1016/j.lithos.2010.01.004

Tapponnier, P., Xu, Z. Q., Roger, F., Meyer, B., Arnaud, N., & Wittlinger, G. (2001). Oblique stepwise rise and growth of the Tibet Plateau. *Science*, *294*(5547), 1671–1677. https://doi.org/10.1126/science.105978

Wang, Q., Niu, F. L., Gao, Y., & Chen, Y. T. (2016). Crustal structure and deformation beneath the NE margin of the Tibetan plateau constrained by teleseismic receiver function data. *Geophysical Journal International*, *204*(1), 167–179. https://doi.org/10.1093/gji/ggv420

Wang, W. L., Wu, J. P., Fang, L. H., Lai, G. J., & Cai, Y. (2017). Sedimentary and crustal thicknesses and Poisson's ratios for the NE Tibetan Plateau and its adjacent regions based on dense seismic arrays. *Earth and Planetary Science Letters*, *462*, 76–85. https://doi.org/10.1016/j.eps1.2016.12.040

Wang, X., Li, Y., Ding, Z., Zhu, L., Wang, C., & Bao, X. (2017). Three-dimensional lithospheric S wave velocity model of the NE Tibetan Plateau and western North China Craton. *Journal of Geophysical Research: Solid Earth*, *122*, 6703–6720. https://doi.org/10.1002/2017JB014203

Wei, X. Z., Jiang, M. M., Liang, X. F., Chen, L., & Ai, Y. S. (2017). Limited southward underthrusting of the Asian lithosphere and material extrusion beneath the northeastern margin of Tibet, inferred from teleseismic Rayleigh wave tomography. *Journal of Geophysical Research: Solid Earth*, *122*, 7172–7189. https://doi.org/10.1002/2016JB013832

Wessel, P., & Smith, W. H. F. (1995). New version of the Generic Mapping Tools released. *Eos, Transactions of the American Geophysical Union*, *76*(33), 329–329. https://doi.org/10.1029/95EO00198

Xu, Q., Zhao, J. M., Yuan, X. H., Liu, H. B., & Pei, S. P. (2017). Detailed configuration of the underthrusting Indian lithosphere beneath western Tibet revealed by receiver function images. *Journal of Geophysical Research: Solid Earth*, *122*, 8257–8269. https://doi.org/10.1002/2017JB014490

Ye, Z., Gao, R., Li, Q. S., Zhang, H. S., Shen, X. Z., & Liu, X. Z. (2015). Seismic evidence for the North China plate underthrusting beneath northeastern Tibet and its implications for plateau growth. *Earth and Planetary Science Letters*, *426*, 109–117. https://doi.org/10.1016/j.epsl.2015.06.024

Yin, A., & Harrison, T. M. (2000). Geologic evolution of the Himalayan-Tibetan orogen. *Annual Review of Earth and Planetary Sciences*, *28*(1), 211–280. https://doi.org/10.1146/annurev.earth.28.1.211.

Yu, X. H., Mo, X. X., Zhao, Z. D., Huang, X. K., Li, Y., Chen, Y. F. (2009). Two types of Cenozoic potassic volcanic rocks in West Qinling, Gansu Province: Their petrology, geochemistry and petrogenesis (in Chinese). *Earth Science Frontiers, 16*(2), 79–89

Yu, Y., & Chen, Y. J. (2016). Seismic anisotropy beneath the southern Ordos block and the Qinling-Dabie orogen, China: Eastward Tibetan asthenospheric flow around the southern Ordos. *Earth and Planetary Science Letters*, *455*, 1–6. https://doi.org/10.1016/j.epsl.2016.08.026

Yuan, D. Y., Ge, W. P., Chen, Z. W., Li, C. Y., Wang, Z. C., & Zhang, H. P. (2013). The growth of northeastern Tibet and its relevance to large-scale continental geodynamics: A review of recent studies. *Tectonics*, *32*, 1358–1370. https://doi.org/10.1002/tect.20081

Yuan, X. H., Kind, R., Li, X. Q., & Wang, R. J. (2006). The S receiver functions: Synthetics and data example. *Geophysical Journal International*, *165*(2), 555–564. https://doi.org/10.1111/j.1365-246X.2006.02885.x

Zhang, P. Z., Shen, Z., Wang, M., Gan, W. J., Burgmann, R., & Molnar, P. (2004). Continuous deformation of the Tibetan Plateau from global positioning system data. *Geology*, *32*(9), 809–812. https://doi.org/10.1130/G20554.1

Zhang, Q., Sandvol, E., Ni, J., Yang, Y. J., & Chen, Y. J. (2011). Rayleigh wave tomography of the northeastern margin of the Tibetan Plateau. *Earth and Planetary Science Letters*, *304*(1–2), 103–112. https://doi.org/10.1016/j.epsl.2011.01.021

Zhang, Z. J., Bai, Z. M., Klemperer, S. L., Tian, X. B., Xu, T., & Chen, Y. (2013). Crustal structure across northeastern Tibet from wide-angle seismic profiling: Constraints on the Caledonian Qilian orogeny and its reactivation. *Tectonophysics*, *606*, 140–159. https://doi.org/10.1016/j.tecto.2013.02.040

Zheng, D., Li, H. Y., Shen, Y., Tan, J., Ouyang, L. B., & Li, X. F. (2016). Crustal and upper mantle structure beneath the northeastern Tibetan Plateau from joint analysis of receiver functions and Rayleigh wave dispersions. *Geophysical Journal International*, *204*(1), 583–590. https://doi.org/10.1093/gji/ggv469

Zheng, X. F., Yao, Z. X., Liang, J. H., & Zheng, J. (2010). The role played and opportunities provided by IGP DMC of China National Seismic Network in Wenchuan earthquake disaster relief and researches. *Bulletin of the Seismological Society of America*, *100*(5B), 2866–2872. https://doi.org/10.1785/0120090257

Zuza, A. V., Cheng, X. G., & Yin, A. (2016). Testing models of Tibetan Plateau formation with Cenozoic shortening estimates across the Qilian Shan-Nan Shan thrust belt. *Geosphere*, *12*(2), 501–532. https://doi.org/10.1130/GES01254.1